Charge Carrier Screening in Photoexcited Epitaxial Semiconductor Nanorods Revealed by Transient X-ray Absorption Linear Dichroism

Thomas C. Rossi,[*,†,†] Conner Dykstra,[‡,†] Tyler N. Haddock,[‡,†] Rachel Wallick,[‡,†] John H. Burke,[‡,†] Cecilia M. Gentle,[‡,†] Gilles Doumy,[¶] Anne Marie March,[¶] and Renske M. van der Veen[*,‡,†,§]

†*Materials Research Laboratory, University of Illinois Urbana-Champaign, Urbana, Illinois 61801, United States*

‡*Department of Chemistry, University of Illinois Urbana-Champaign, Urbana, Illinois 61801, United States*

¶*Chemical Sciences and Engineering Division, Argonne National Laboratory, 9700 S. Cass Ave., Lemont, Illinois 60439, United States*

§*Department of Materials Science & Engineering, University of Illinois Urbana-Champaign, Urbana, Illinois 61801, United States*

E-mail: thomas.rossi@helmholtz-berlin.de; renske.vanderveen@helmholtz-berlin.de

Abstract

Understanding the electronic structure and dynamics of semiconducting nanomaterials at the atomic level is crucial for the realization and optimization of devices in solar energy, catalysis, and opto-electronic applications. We report here on the use of ultrafast X-ray linear dichroism spectroscopy to unravel the carrier dynamics in epitaxial ZnO nanorods after band-gap photoexcitation. By rigorously subtracting out thermal contributions and conducting *ab initio* calculations, we reveal an overall depletion of absorption cross sections in the transient X-ray spectra caused by photogenerated charge carriers screening the core-hole potential of the X-ray absorbing atom. At low laser excitation densities, we observe phase-space filling by excited electrons and holes separately. These results pave the way for carrier- and element-specific probing of charge transfer dynamics across heterostructured interfaces with ultrafast table-top and fourth generation X-ray sources.

Keywords

Semiconductors, nanorods, zinc oxide, X-ray spectroscopy, carrier dynamics, screening

Introduction

The past decade has seen the development of photovoltaic cells with great chemical and structural complexity. Highly-ordered epitaxial nanorods are promising alternatives to the mesoporous nanoparticle thin films in dye-sensitized[1] and perovskite-sensitized solar cells.[2] Zinc oxide (ZnO) nanorods in particular, have emerged as promising candidates for unidimensional electron transport due to their low-cost, high optical transparency,[3] relatively high electron mobility,[4] and production through simple solution-based techniques.[5,6] The directional carrier transport can be enhanced by the piezotronic properties of ZnO[7,8] upon deformation,[9] which calls for a deeper understanding of the interplay between excited charge carriers and the local/non-local electronic and lattice structure of semiconductors.

X-ray transient absorption (XTA) spectroscopy, has become a powerful tool at third-generation synchrotrons and X-ray free electron lasers (XFELs) for the study of excited-state dynamics in solids, and nanostructures[10] at the atomic level of multiple element materials.[11] Combined with X-ray linear dichroism (XLD),[12] XTA can become sensitive to anisotropic changes in the electronic and lattice structure upon semiconductor photoexcitation. A major limitation of XTA to the study of photovoltaic materials is its apparent lack of sensitivity to delocalized charge carriers. Previous XTA studies on semiconducting (nano)materials have primarily reported *local* effects, such as polaron formation,[11,13–16] carrier trapping,[17–20] lattice expansion,[21] Jahn-Teller[22] or piezoelectric[23] distortion, and change of valence states.[24–27] Furthermore, lattice heating arising from laser excitation is often neglected, despite appreciable temperature rises in excited nanoscale and thin-film materials on the picosecond (ps) timescale[21,28] which are often reported by time-resolved X-ray diffraction (XRD).[29]

Here, we use transient ps-resolved XLD to reveal *non-local* electronic effects in the Zn K-edge XAS of photoexcited epitaxial ZnO nanorods as a fingerprint of carrier transport. We first benchmark the photothermal temperature rise by static temperature-dependent XAS and show that heating contributions cancel out in the transient XLD spectrum. The comparison between *ab initio* X-ray absorption simulations including and omitting a $1s$ core-hole suggests that the non-thermal transient XANES is dominated by screening/shielding of the core-hole potential by photogenerated mobile charge carriers. While such effects are known to influence static XAS spectra,[30,31] here we show for the first time that variations in

core-hole screening caused by free charge carriers significantly contribute to *transient* X-ray spectra of photoexcited semiconductors. Furthermore, at the lowest laser fluence, we observe well-separated signatures of excited hole and electron carriers across the band gap due to phase-space filling (PSF). Overall, these observations have important implications for the use of ultrafast XAS in elucidating the dynamics of free, dressed, and trapped charge carriers in semiconductor nano(hetero)structures for photovoltaic applications.

Results and Discussion

The samples consist of epitaxial wurtzite ZnO nanorods (1–2 μm long, 67$\pm$14 nm wide) on monocrystalline quartz substrates. Figure 1a shows top- and side-view scanning electron microscopy (SEM) images of the nanorods. The synthesis procedure is provided in the Supporting Information 1 and detailed characterizations are given in Supporting Information 2. The nanorods are primarily oriented along the **c**-axis, which is confirmed by a single (001) reflection observed in the XRD pattern (Figure 1b). Figure 1d shows the Zn K-edge XAS with an incidence angle of 90° (normal) and 45° (diagonal) between the X-ray polarization and the crystal **c**-axis (see also Figure 1c for the experimental setup). The resulting XLD spectra (diagonal minus normal incidence) at room temperature (RT, 25 $^\circ$C) and 70 $^\circ$C are also depicted (see Supporting Information 2.4 for details of the data correction and normalization procedures, Figure S4 for a detailed XLD measurement in small angular steps, and Figure S5 for comparison with the literature). The XANES primarily consists of dipole-allowed 1s$\rightarrow$4p transitions and transitions to the continuum.[32] Weak pre-edge features arising from dipole-forbidden 1s$\rightarrow$3d transitions may emerge due to oxygen vacancies in semiconducting metal oxides.[33] The absence of such features in the present XAS spectrum evidences a low oxygen vacancy concentration, in agreement with XPS and photoluminescence measurements (Supporting Information 2.3 and 2.5). The strong XLD in the XANES spectrum is due to anisotropy in bond lengths of the σ Zn-O bonds in the (**a**,**b**)-plane and the π-bonds along the **c**-axis.[34,35]

Figure 1c schematically shows the geometry for static and transient XLD experiments (see Supporting information 1.2 and 1.3 for details). Laser pump (355 nm, $\sim$10 ps) and X-ray probe ($\sim$70 ps) pulses were

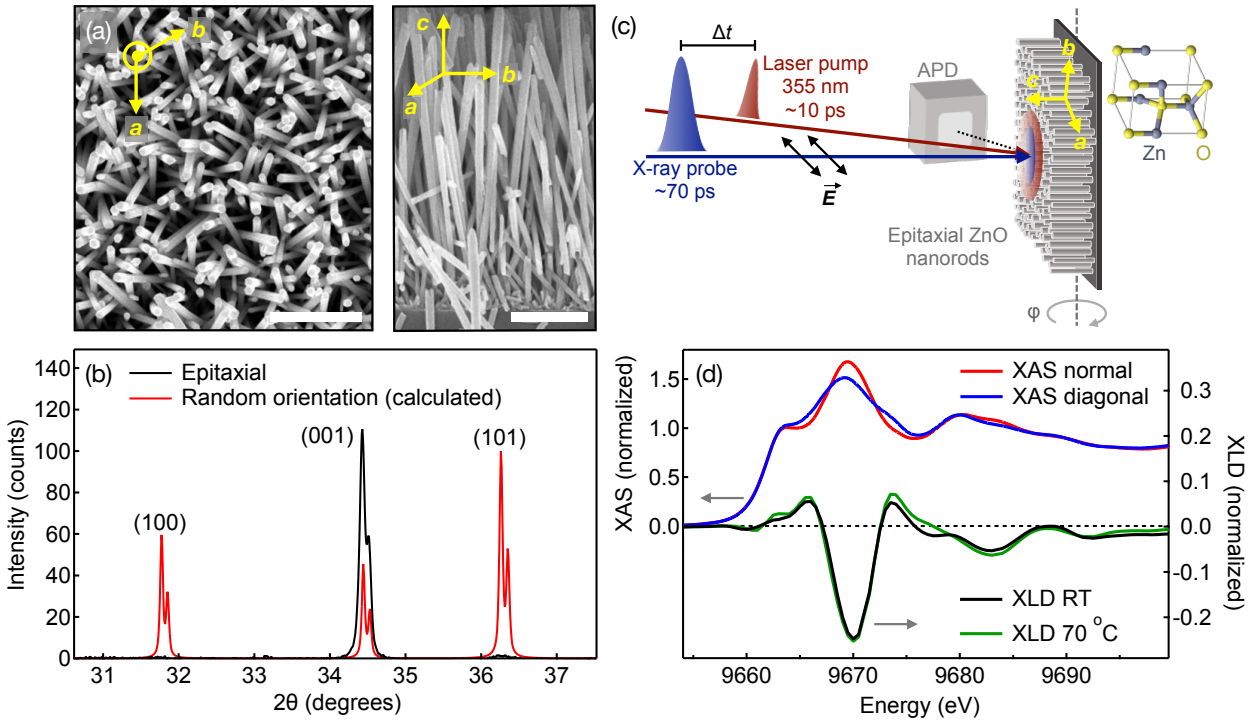

Figure 1: (a) Top- and side-view SEM images of the epitaxial ZnO nanorods. The relative orientation of the wurtzite unit cell lattice vectors is shown in yellow. The white scale bars represent 1 μm; (b) XRD of the epitaxial nanorods on a quartz substrate (black) with the calculated pattern for a random orientation distribution of wurtzite unit cells (red); (c) Schematics of the laser pump – X-ray linear dichroism (XLD) probe experiment. The sample is rotated around an axis (angle ϕ) such that the electric field vector of the X-rays ($\vec{E}$) makes an angle of 90° (normal) or 45° (diagonal) with the **c**-axis. X-ray fluorescence is detected using two APDs at ~85° relative to the X-ray beam (only one shown). The ZnO unit cell is schematically shown on the right. A similar setup was used for the static XLD measurements, but without laser excitation; (d) Normalized Zn K-edge XAS of the nanorods at normal (red) and diagonal (blue) incidence (left axis). XLD at room temperature (RT; black) and at 70 °C (green) (right axis).

delivered to the sample in near-collinear geometry (5° relative angle). The incident laser fluence (0.2 to 7.3 mJ/cm^2, calculated with 1/e^2 beam diameter) was kept relatively low to minimize heating and sample damage. More details about the beam alignment procedure, calibration, and sample damaging tests are provided in Supporting Information 3.

Figure 2a shows the XTA spectra in the XANES at normal and diagonal incidence at ~100 ps after photoexcitation at a similar laser excitation density of ~3·10^{19} cm^{-3} (see Supporting Information 4 for details on excitation densities). All forthcoming XTA spectra are normalized to the XAS edge jump. In both spectra, the transient shows a pronounced bleach at ~9670 eV with positive wings at 9660-9665 and ~9675 eV. The XTA spectra at normal and diagonal incidence exhibit clear differences, in particular

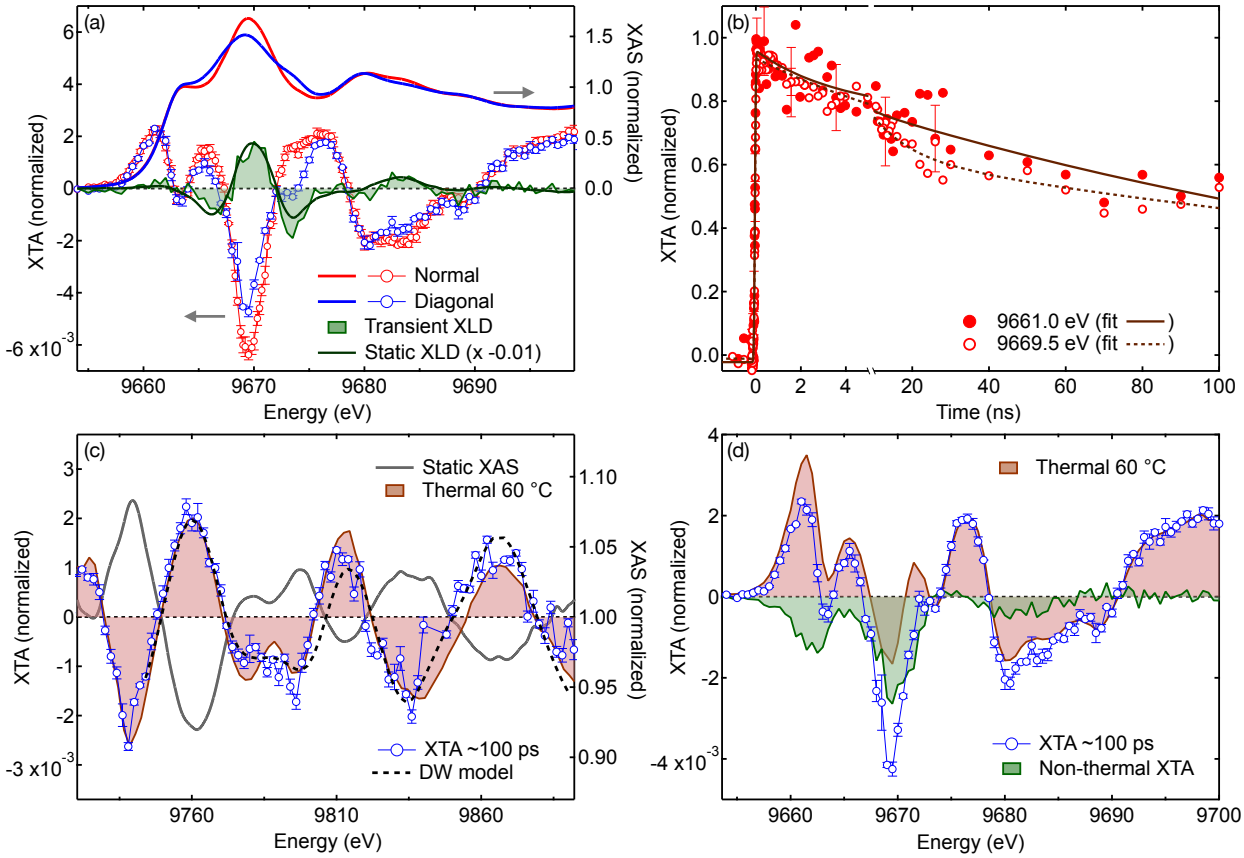

Figure 2: (a) Transient XANES at normal (red circles) and diagonal (blue circles) incidence at ∼100 ps after photoexcitation at 355 nm with an excitation density of $\sim 3 \cdot 10^{19}$ cm^{-3} (left axis). The resulting transient XLD spectrum (diagonal-normal) is shown in shaded green (left axis). The inverted static XLD spectrum (scaled by 0.01) is shown with a solid black curve. The XAS at normal (solid red) and diagonal (solid blue) incidence are shown for reference (right axis). Note that the static XLD spectrum in this figure slightly deviates from the one in Figure 1d due to small differences in the static spectra of the two different samples. Error bars are ± standard deviations between individual measurements (applies to all forthcoming plots). (b) Normalized time traces at normal incidence at 9661 eV (filled circles) and 9669.5 eV (open circles) for a fluence of 7.3 mJ/cm^2 (a few error bars are shown for reference). Biexponential fittings are shown with continuous and dashed lines at the respective energies. (c) Transient EXAFS spectrum at diagonal incidence at ∼100 ps after photoexcitation at 355 nm and 6.1 mJ/cm^2 (blue circles). Simulated static difference spectrum for a lattice temperature of 60 °C (red shaded curve). Calculated difference spectrum for a Zn Debye-Waller (DW) factor increase of 0.54 mÅ^2 (black dashed curve). The static EXAFS spectrum is shown for reference (gray curve); (d) Transient XANES spectrum at diagonal incidence at ∼100 ps after photoexcitation at 355 nm and 6.1 mJ/cm^2 (blue circles). Simulated static difference spectrum for a lattice temperature of 60 °C (red shaded curve). The difference between the experimental transient (blue) and the thermal difference spectrum (red) results in the non-thermal XTA spectrum (green shaded curve).

between 9665 and 9675 eV, which constitute the transient XLD spectrum. Figure 2b shows time traces at normal incidence and at two different energies (9661 and 9669.5 eV). A biexponential fitting indicates that the transient signal recovers with two time constants of 1–10 ns and 200–300 ns, independent of the

energy within the confidence intervals. The shorter process is assigned to carrier recombination based on the similarity with the band-edge photoluminescence lifetime, and the longer time scale is assigned to heat dissipation (Supporting Information 5).

Calibration of Photothermal Effects in Transient X-ray Absorption Spectroscopy. We briefly discuss the extent of laser-induced heating in the XTA spectra. The slight excess energy ($\sim$10 meV) introduced into the carriers by photoexcitation at 355 nm (see Supporting Information 2.5), is transferred to the phonon bath by carrier-phonon scattering within $<$500 fs.[36] A temperature rise of the ZnO lattice is expected on the $\sim$100 ps time scale due to a large interfacial thermal resistance with air and the substrate.

Figure 2c shows the transient EXAFS at $\sim$100 ps after photoexcitation at 6.1 mJ/cm^2 (diagonal incidence). The transient shows oscillations with the same periodicity and opposite sign as the static spectrum, which indicates a mere damping of the EXAFS oscillations in the photoexcited state. This damping is due to an increased amplitude of the incoherent vibrational motion of atoms in a warmer lattice, and can be accounted for using a Debye-Waller (DW) factor.[37,38] No changes in the frequency of the EXAFS modulations are observed implying that no significant bond length changes occur in the vicinity of the Zn atoms after photoexcitation. The transient EXAFS can thus be used to accurately calibrate the lattice temperature as a result of laser heating, which is then used in the analysis of the transient XANES spectrum. The temperature calibration is based on the measurement of XAS between RT and 500 $^\circ$C with small temperature increments, following a similar procedure as Mahl and coworkers on laser-excited CuO at the O K-edge[28] (detail in Supporting Information 6.1). The excited-state lattice temperatures derived by this method are summarized in Table S4 (Supporting Information 6.2). A best-match example is given in Figure 2c for a corresponding lattice temperature of 60 $^\circ$C in the excited state. We note that even for relatively moderate laser fluences of a few mJ/cm^2, appreciable temperature increases of tens of degrees occur. This analysis is corroborated by full-multiple scattering calculations (Supporting Information 6.1). In Supporting Information 7, we show that the excited carrier density is homogeneously distributed across the nanorod volume in $<$3 ps, leading to a homogeneous lattice heating of the nanorods $\sim$100 ps after photoexcitation. The warm nanorod lattice can therefore be modeled by a single temperature despite the large mismatch between the laser and X-ray penetration depth of $\sim$110 nm and $\sim$8.5 μm,[39] respectively.

The analysis of the transient EXAFS demonstrates the absence of large changes in Zn–O bond distance and therefore excludes the formation of hole polarons[40] and trapped holes[41] in the epitaxial ZnO nanorods studied here.

Non-Thermal Transient XANES and X-ray Linear Dichroism. We now use the calibration of the lattice temperature to establish the non-thermal contributions in the transient XANES. Figure 2d shows the transient XANES at diagonal incidence ($\sim$100 ps, fluence 6.1 mJ/cm^2) together with the static difference spectrum at 60$\pm$5 °C, which is the lattice temperature determined in the transient EXAFS analysis for these conditions (Figure 2c). By subtracting the thermal difference spectrum from the $\sim$100 ps transient XANES spectrum, we obtain the non-thermal XTA spectrum (green shaded curve in Figure 2d). The XTA decomposition into thermal and non-thermal contributions is readily extended to different angles of incidence and excitation fluences (Supporting Information Figures S15 and S16). This separation shows that positive features in the transient XANES originate from increased lattice temperature. In particular, the first positive peak at $\sim$9660 eV in the transient matches the shape of the thermal contribution while it could be mistaken for a red shift of the edge as a result of charge trapping (Supporting Information 8). Interestingly, as seen in Figure 2d, the non-thermal transient XANES at $\sim$100 ps is characterized by a purely negative triple-peak structure centered at and above the absorption edge.

To corroborate these findings, we return to the XLD spectra. First, the static XLD spectrum does not significantly depend on temperature in the range RT–70 °C (Figure 1d and Supporting Information Figure S13). This means that the laser-induced heating effects effectively cancel out in the transient XLD spectrum. Second, the *transient* XLD spectrum resembles the scaled inverted *static* XLD spectrum (Figure 2a), confirming the existence of an excited-state process that leads to a mere depletion of the absorption cross-section in the XANES (mathematical justification and additional data in Supporting Information 10). Figure 3 illustrates this in more detail by showing the non-thermal XTA spectra at diagonal incidence at various laser fluences (similar plots at normal incidence in Supporting Information 6). The amplitude of the bleach features at $\sim$9663 and $\sim$9670 eV increases linearly with pump fluence above $\sim$2 mJ/cm^2 (see Figure S26a and Supporting Information 11). Since the amplitude of the entire XTA signal scales linearly with pump fluence above $\sim$2 mJ/cm^2 (Figure S26b), we conclude that both thermal and non-thermal

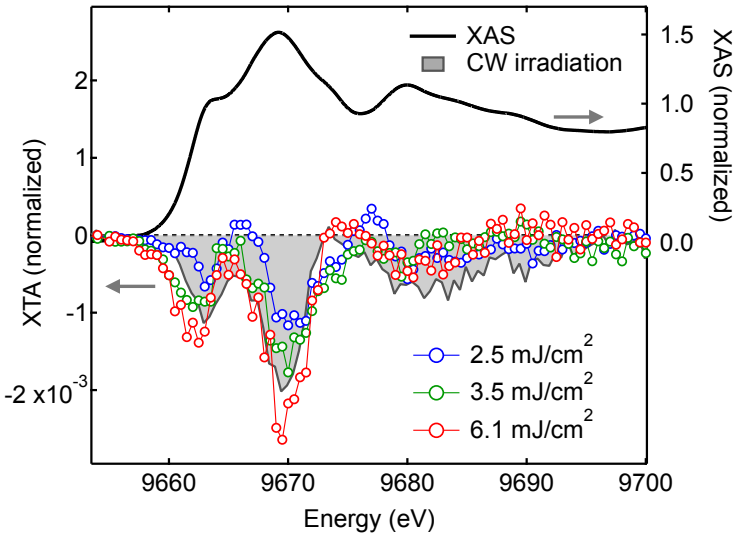

Figure 3: Non-thermal XTA spectra at diagonal incidence (colored circles, left axis). The static XAS is provided with a black line for reference (right axis). The difference XAS of ZnO nanorods under solar illumination with respect to a dark spectrum is provided for comparison (gray shaded curve, scaled arbitrarily, adapted from Chen et al.[42]).

contributions scale linearly with pump fluence in this range.

The transient EXAFS analysis described above ruled out significant structural distortions in the vicinity of the Zn atoms in the excited state. We therefore interpret the non-thermal transient XLD/XANES spectrum as originating from excited *free*, *delocalized* carriers (as opposed to *trapped* carriers). Interestingly, Figure 3 shows that the non-thermal transient at diagonal incidence resembles a difference spectrum obtained under continuous light irradiation of ZnO nanorods (grey shaded curve, adapted from ref.[42]) or other sensitized ZnO nanomaterials[42–45] (see Supporting Information 12). We thus conclude that the non-thermal XTA spectrum is dominated by the effect of free electrons photoexcited in the conduction band of ZnO, as opposed to trapped holes previously reported for photoexcited ZnO nanoparticles.[19]

Non-Local Core-Hole Screening by Excited Charge Carriers. To explain the depletion of XANES spectral intensity by delocalized photoexcited electrons, we invoke the effect of Coulomb screening in core-level spectroscopy.[46–48] Absorption of an X-ray photon leaves a hole in the 1s core orbital (core-hole), which causes a rearrangement of the valence electrons and a contraction of the unoccupied energy levels. The overall effect is a partial shielding, or screening, of the core-hole Coulomb potential. In the XAS spectrum, such final-state screening effects are visible as changes in the peak position (chemical

shifts)[48,49] and absorption cross-section (XAS intensity).[48] Based on these findings, we propose that the photoexcited electrons in the conduction band of ZnO increase the screening of the core-hole interaction, causing a renormalization of the dipole matrix elements (*i.e.* cross-sections) of the transitions to the 4p-DOS and to the continuum which represents a many-body non-local screening effect in the XAS final state. In ZnO, hole screening can be neglected due to the difference in effective masses ($m_e^* = 0.23\ m_0$[50] and $m_h^* = 3.6\ m_0$,[51] with m_0 the electron rest mass[1]).

***Ab Initio* XAS Calculations.** To support our interpretation, we performed *ab initio* self-consistent single-particle XAS calculations at the Zn K-edge with a static fully-screened core-hole and without a core-hole (see Supporting Information 1.4 and 13 for details). The comparison between two extreme cases (hole and no hole) is used to qualitatively investigate the effect of a suppressed interaction between the core-hole and the valence electrons due to the strong screening of the core-hole potential common in transition metal oxides.[47,52] Figure 4a shows the XANES spectra calculated using the real-space density functional theory (DFT)-based FDMNES code.[53] When the core-hole is present, the spectrum is red shifted and the XANES intensity close to the ionization threshold is enhanced as expected from the evolution of the wave-functions.[54] The calculated difference spectrum (without minus with core-hole) in Figure 4a shows a net negative signal, qualitatively matching the experimental non-thermal XTA spectrum. Similar results were obtained using the reciprocal-space DFT-based XSpectra code[55] (Figure S35). The enhanced screening of the core-hole potential predominantly depletes the X-ray absorption cross-section, while the edge shift plays a subordinate role. The theoretical and experimental difference spectra show moderate agreement because of i) discrepancies in the calculation of static spectra (which could be improved by employing the Bethe-Salpeter equation[56,57]) and ii) the genuine screening effect is only partial and highly dynamic.[58,59] Overall, these discrepancies are expected to be independent of the X-ray polarization used in the calculation. Figure 4b compares the theoretical difference XLD spectrum with the experimental transient XLD spectrum for an excitation density of $\sim 3 \cdot 10^{19}$ cm^{-3}. Indeed, we find an excellent agreement which shows that the errors between calculations at normal and diagonal incidence cancel out in the difference XLD spectrum. Theoretical XAS codes can thus predict transient XLD signals, despite significant theoretical

[1] Average effective masses along the ordinary and extraordinary directions.

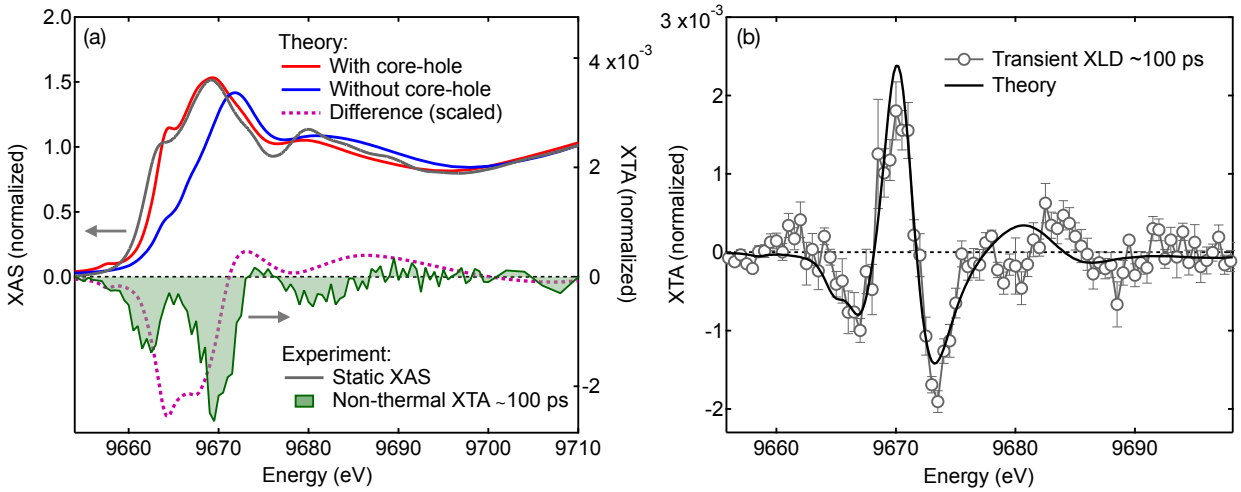

Figure 4: (a) Calculated Zn K-edge XAS of ZnO at diagonal incidence with core-hole (red line) and without core-hole (blue line) using the FDMNES code,[53] and the resulting scaled difference spectrum (without minus with core-hole, pink dashed line). The normalized experimental XAS at diagonal incidence is shown for comparison (all left axis). The non-thermal transient XANES spectrum at diagonal incidence (∼100 ps, 3.5 mJ/cm^2) is shown as a shaded green curve (right axis); (b) Experimental transient XLD spectrum at ∼100 ps (gray circles, excitation density ∼3·10^{19} cm^{-3}) and the calculated difference XLD spectrum (black curve, difference between pink dashed curve in panel (a) and the one in Figure S32b). The calculated difference spectrum has been scaled to match the amplitude of the experimental spectrum.

errors due to, *e.g.*, many-body effects.

Phase-Space Filling by Excited Electrons and Holes. The non-local core-hole screening discussed above plays a major role for electron densities of >5·10^{18} cm^{-3} comparable to the Mott density.[60,61] At lower laser fluences and densities (<1 mJ/cm^2, <1·10^{18} cm^{-3}), both thermal and core-hole screening effects are diminished and transient phase-space filling (PSF) by excited charge carriers becomes visible in the XTA spectrum. PSF (or Pauli blocking) refers to the occupation of the conduction band by electrons and the valence band by holes, giving rise to a decreased (bleached) or increased photoabsorption cross-section, respectively. Transient PSF has been previously observed at L-[62,63] and M-edges.[64–67]

Figure 5a shows the transient XTA spectrum at normal incidence and at low laser fluence (∼0.2 mJ/cm^2 [2]), together with the scaled XTA spectrum at higher fluence (3.0 mJ/cm^2) for comparison. The absence of any positive features at ∼9661, ∼9665, and ∼9677 eV (marked with arrows in Figure 5a) shows that thermal effects are negligible at fluences of ∼0.2 mJ/cm^2. In addition, the negative features

[2]The presence of residual harmonics used to generate the 355 nm pump beam compromises the accuracy of fluence estimates <1 mJ/cm^2.

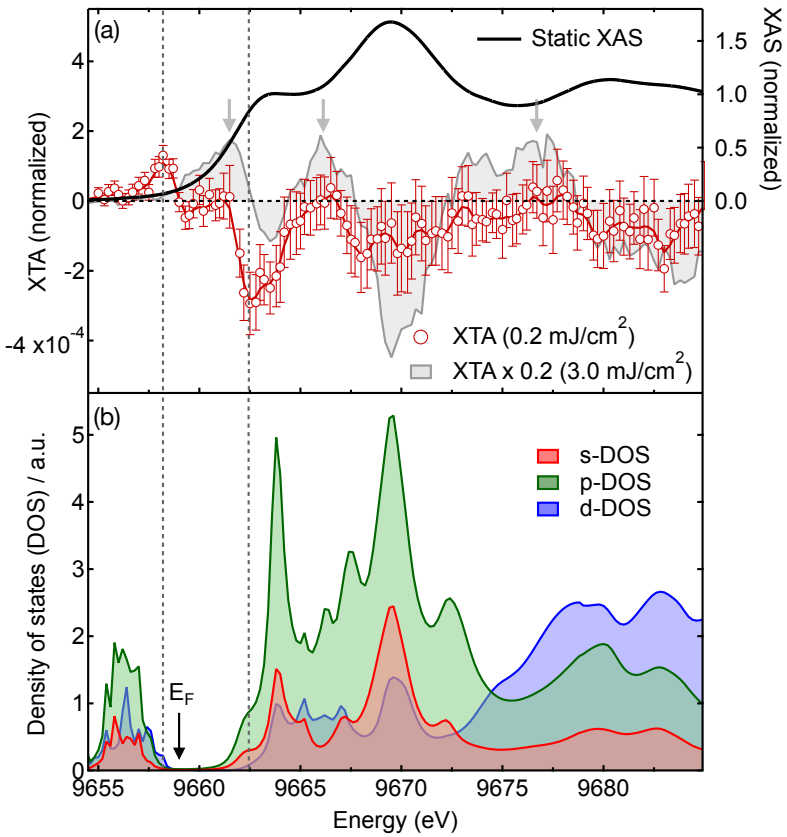

Figure 5: (a) XTA spectra at normal incidence, ∼100 ps, low laser fluence (∼0.2 mJ/cm^2, red circles) and higher laser fluence (3.0 mJ/cm^2, scaled by 0.2, gray shaded curve, both left axis). The solid red line is a trendline. The experimental static XAS is shown with a black curve for reference (right axis). (b) Calculated Zn s-projected (shaded red), p-projected (shaded green), and d-projected (shaded blue) DOS with core-hole calculated with the FDMNES code. Vertical dashed lines are centered at the PSF features in the low-fluence XTA. The Fermi energy is indicated in (b) by an arrow.

around ∼9670 and ∼9682 eV indicate only a small (∼20%, see Figure S26a) contribution from transient core-hole screening. Interestingly, the amplitude ratio of the two bleach features around 9662.5 eV and 9670 eV clearly depends on laser fluence; the low-energy bleach feature is larger than the high-energy one in the low fluence data set (Figure 5a) and *vice versa* for the high-fluence data set (Figures 2d and 3). Furthermore, at even lower energy (∼9658 eV), and separated by a region with no signal, a weak positive feature appears that has not been discernable in the high-fluence data sets because it was submerged by the strong thermal peak around ∼9661 eV.

In Figure 5b, we show that the position of these features (vertical dashed lines) matches the band edges in the Zn l-projected DOS calculated with the FDMNES code[53] in the presence of a core-hole

(see Supporting Information 13.1 for the DOS calculated without a core-hole). In ZnO, Zn atoms are in a tetrahedral environment, hence K-edge transitions to s- or d-states become partially allowed through hybridization with the p-DOS. The positive feature is therefore attributed to excited hole carriers at the top of the valence band below the Fermi level (E_F), which gains intensity through hybridization of Zn d- and p-states, while the negative feature around $\sim$9662.5 eV is (partially) due to PSF of excited electrons in states of p-symmetry at the bottom of the conduction band. The bleach features at higher energies ($\sim$10–20 eV above E_F) cannot be due to PSF since the population of such states would require exceedingly large carrier densities and hot carrier populations; these features are due to transient core-hole screening instead.

Conclusions

Our results demonstrate the use of ps-resolved transition-metal K-edge spectroscopy to track the evolution of excited charge carriers in a widely used prototypical ZnO semiconducting material.[68,69] We use transient XLD as a new methodology to isolate non-thermal contributions in the transient XANES. Our approach revealed, for the first time, the screening of the core-hole potential by delocalized excited electrons in the transient XAS of photoexcited semiconducting materials. These results are in contrast with a large body of previous ultrafast XAS studies on semiconducting materials that report on charge trapping and/or polaron formation upon photoexcitation. Our results thus have profound implications for future pump-probe and quasi-equilibrium XAS studies on photovoltaic and photocatalytic nanomaterials.[42–45]

The methodology presented here paves the way for the study of charge transfer dynamics in more complex heterostructured materials and devices such as dye- or quantum dot-sensitized nanomaterials, multilayered thin films, or solid/liquid interfaces in photoelectrochemical cells. The element specificity of hard X-ray spectroscopy enables the selective tracking of charge transfer across heterostructured interfaces. We show here that phase-space filling in the pre-edge XAS region can be used to track electrons and holes separately. In addition, the future use of transient X-ray linear dichroism may yield information on the anisotropy of carrier screening, transfer, and trapping in photoexcited strongly dichroic materials

such as transition metal dichalcogenides,[70] 2D lead halide perovskites,[71] or layered materials.[72] Finally, extending these studies to the femtosecond time regime at X-ray free electron lasers and table-top instruments offers an exciting perspective for the study of ultrafast processes such as hot carrier injection, carrier cooling, and trapping in nanoscale solar energy materials.

Supporting Information Available

The Supporting Information is available free of charge which contains sample synthesis and characterizations, experimental details about the XTA measurements, calculation of the excitation densities, additional kinetics, evolution of XAS with lattice temperature, simulation of the timescale of heat diffusion, effect of the penetration depth mismatch between the laser and the X-rays, chemical shift simulations, thermal and screening effects in previous XTA measurements at the metal K-edge, mathematical derivation of transient XLD, XTA fluence dependence, XAS of ZnO under solar illumination – non-local screening effects, *ab initio* calculations.

Author Information

Corresponding Authors

*E-mail: renske@alumni.ethz.ch

*E-mail: thomas.rossi@helmholtz-berlin.de

Present Address

Renske M. van der Veen & Thomas C. Rossi: Department Atomic-Scale Dynamics in Light-Energy Conversion, Helmholtz-Zentrum für Materialien und Energie GmbH, Magnusstraße 2, 12489 Berlin, Germany

ORCID

Renske M. van der Veen: 0000-0003-0584-4045

Thomas C. Rossi: 0000-0002-7448-8948

Cecilia M. Gentle: 0000-0002-5364-3830

John H. Burke: 0000-0001-9853-7292

Conner Dykstra: 0000-0001-5597-6914

Tyler N. Haddock: 0000-0002-8116-145X

Rachel Wallick: 0000-0002-7548-4850

Gilles Doumy: 0000-0001-8672-4138

Anne Marie March: 0000-0003-2961-1246

Notes

The authors declare no competing financial interest.

Acknowledgement

We would like to thank Rick Haasch for help with the XPS measurements. Don Walko and Christopher J. Otolski for help during the beamtime. We thank Ernest P. Northen for the machining of the chamber used in the experiment. We thank Prof. Andre Schleife for fruitful discussions. We thank Hao Ming Chen for providing us with the XAS data of ZnO nanorods under solar illuminations previously published in.[42] We thank Tim Fister and Yang Ren for providing the Linkam oven during the beamtime. Part of the measurements were carried out in the Material Research Laboratory Central Research Facilities at the University of Illinois Urbana-Champaign, partially supported by NSF through the University of Illinois Materials Research Science and Engineering Center DMR-1720633. This work made use of the Illinois Campus Cluster, a computing resource that is operated by the Illinois Campus Cluster Program (ICCP) in conjunction with the National Center for Supercomputing Applications (NCSA) and which is supported by funds from the University of Illinois at Urbana-Champaign. We acknowledge funding from the David and Lucile Packard Foundation, the ACS Petroleum Research Fund (#59410-DNI6), and the Solar Photochemistry Program of the Department of Energy (DE-SC0021062). Co-author T.N.H. was funded by the National Science Foundation through award no. 1751725. This research used resources of the Advanced Photon Source, a U.S. Department of Energy (DOE) Office of Science User Facility operated for the DOE Office of Science by Argonne National Laboratory under contract no. DE-AC02-06CH11357. We are grateful to the staff of 7-ID from the APS for help during the experiment. A. M. March and G. Doumy were supported by the US Department of Energy, Office of Science, Office of Basic Energy Sciences, Chemical Sciences, Geosciences and Biosciences Division under award number DE-AC02-06CH11357.

References

(1) Kalyanasundaram, K. Applications of functionalized transition metal complexes in photonic and optoelectronic devices. *Coordination Chemistry Reviews* **1998**, *177*, 347–414.

(2) Selim, M. S.; Elseman, A. M.; Hao, Z. ZnO Nanorods: An Advanced Cathode Buffer Layer for Inverted Perovskite Solar Cells. *ACS Applied Energy Materials* **2020**, *3*, 11781–11791.

(3) Fujiwara, H.; Kondo, M. Effects of carrier concentration on the dielectric function of ZnO:Ga and In2O3:Sn studied by spectroscopic ellipsometry: Analysis of free-carrier and band-edge absorption. *Physical Review B* **2005**, *71*, 075109–075110.

(4) Thiemann, S.; Gruber, M.; Lokteva, I.; Hirschmann, J.; Halik, M.; Zaumseil, J. High-Mobility ZnO Nanorod Field-Effect Transistors by Self-Alignment and Electrolyte-Gating. *ACS Applied Materials & Interfaces* **2013**, *5*, 1656–1662.

(5) Fujiwara, H.; Suzuki, T.; Niyuki, R.; Sasaki, K. ZnO nanorod array random lasers fabricated by a laser-induced hydrothermal synthesis. *New Journal of Physics* **2016**, *18*, 103046.

(6) Edley, M. E.; Li, S.; Guglietta, G. W.; Majidi, H.; Baxter, J. B. Ultrafast Charge Carrier Dynamics in Extremely Thin Absorber (ETA) Solar Cells Consisting of CdSe-Coated ZnO Nanowires. *The Journal of Physical Chemistry C* **2016**, *120*, 19504–19512.

(7) Wu, W.; Wang, Z. L. Piezotronics and piezo-phototronics for adaptive electronics and optoelectronics. *Nature Reviews Materials* **2016**, *1*, 1–17.

(8) Pan, C.; Zhai, J.; Wang, Z. L. Piezotronics and Piezo-phototronics of Third Generation Semiconductor Nanowires. *Chemical Reviews* **2019**, *119*, 9303–9359.

(9) Zhang, Y.; Yang, Y.; Wang, Z. L. Piezo-phototronics effect on nano/microwire solar cells. *Energy & Environmental Science* **2012**, *5*, 6850.

(10) Asakura, K.; Gaffney, K. J.; Milne, C.; Yabashi, M. XFELs: cutting edge X-ray light for chemical and material sciences. *Physical Chemistry Chemical Physics* **2020**, *22*, 2612–2614.

(11) Santomauro, F. G. et al. Localized holes and delocalized electrons in photoexcited inorganic perovskites: Watching each atomic actor by picosecond X-ray absorption spectroscopy. *Structural Dynamics* **2017**, *4*, 044002.

(12) Brouder, C. Angular dependence of X-ray absorption spectra. *Journal of Physics: Condensed Matter* **1990**, *2*, 701–738.

(13) Katz, J.; Zhang, X.; Attenkofer, K.; Chapman, K.; Frandsen, C.; Zarzycki, P.; Rosso, K.; Falcone, R.; Waychunas, G.; Gilbert, B. Electron small polarons and their mobility in iron (oxyhydr)oxide nanoparticles. *Science* **2012**, *337*, 1200–1203.

(14) Zheng, K.; Abdellah, M.; Zhu, Q.; Kong, Q.; Jennings, G.; Kurtz, C. A.; Messing, M. E.; Niu, Y.; Gosztola, D. J.; Al-Marri, M. J.; Zhang, X.; Pullerits, T.; Canton, S. E. Direct Experimental Evidence for Photoinduced Strong-Coupling Polarons in Organolead Halide Perovskite Nanoparticles. *The Journal of Physical Chemistry Letters* **2016**, *7*, 4535–4539.

(15) Liu, C.; Tsai, H.; Nie, W.; Gosztola, D. J.; Zhang, X. Direct Spectroscopic Observation of the Hole Polaron in Lead Halide Perovskites. *The Journal of Physical Chemistry Letters* **2020**, *11*, 6256–6261.

(16) Cannelli, O. et al. Quantifying Photoinduced Polaronic Distortions in Inorganic Lead Halide Perovskite Nanocrystals. *J Am Chem Soc* **2021**, *143*, 9048–9059.

(17) Santomauro, F. G. et al. Femtosecond X-ray absorption study of electron localization in photoexcited anatase TiO2. *Scientific Reports* **2015**, *5*, 14834.

(18) Obara, Y.; Ito, H.; Ito, T.; Kurahashi, N.; Thürmer, S.; Tanaka, H.; Katayama, T.; Togashi, T.; Owada, S.; Yamamoto, Y.-i.; Karashima, S.; Nishitani, J.; Yabashi, M.; Suzuki, T.; Misawa, K. Femtosecond time-resolved X-ray absorption spectroscopy of anatase TiO2 nanoparticles using XFEL. *Structural Dynamics* **2017**, *4*, 044033.

(19) Penfold, T. J.; Szlachetko, J.; Santomauro, F. G.; Britz, A.; Gawelda, W.; Doumy, G.; March, A. M.;

Southworth, S. H.; Rittmann, J.; Abela, R.; Chergui, M.; Milne, C. J. Revealing hole trapping in zinc oxide nanoparticles by time-resolved X-ray spectroscopy. *Nature Communications* **2018**, *9*, 478.

(20) Koide, A. et al. Photoinduced anisotropic distortion as the electron trapping site of tungsten trioxide by ultrafast W L1-edge X-ray absorption spectroscopy with full potential multiple scattering calculations. *Physical Chemistry Chemical Physics* **2020**, *22*, 2615–2621.

(21) Hayes, D.; Hadt, R. G.; Emery, J. D.; Cordones, A. A.; Martinson, A. B. F.; Shelby, M. L.; Fransted, K. A.; Dahlberg, P. D.; Hong, J.; Zhang, X.; Kong, Q.; Schoenlein, R. W.; Chen, L. X. Electronic and nuclear contributions to time-resolved optical and X-ray absorption spectra of hematite and insights into photoelectrochemical performance. *Energy & Environmental Science* **2016**, *9*, 3754–3769.

(22) Vorobeva, E.; Johnson, S. L.; Beaud, P.; Milne, C. J.; Benfatto, M.; Ingold, G. Local structural changes in excited Ti3+:Al2O3 studied by time-resolved XANES. *Physical Review B* **2009**, *80*, 134301–134306.

(23) Wen, H.; Sassi, M.; Luo, Z.; Adamo, C.; Schlom, D. G.; Rosso, K. M.; Zhang, X. Capturing ultrafast photoinduced local structural distortions of BiFeO3. *Scientific Reports* **2015**, *5*, 15098.

(24) Katz, J. E.; Gilbert, B.; Zhang, X.; Attenkofer, K.; Falcone, R. W.; Waychunas, G. A. Observation of Transient Iron(II) Formation in Dye-Sensitized Iron Oxide Nanoparticles by Time-Resolved X-ray Spectroscopy. *The Journal of Physical Chemistry Letters* **2010**, *1*, 1372–1376.

(25) Uemura, Y. et al. Dynamics of Photoelectrons and Structural Changes of Tungsten Trioxide Observed by Femtosecond Transient XAFS. *Angewandte Chemie* **2016**, *128*, 1386–1389.

(26) Hassan, A.; Zhang, X.; Liu, X.; Rowland, C. E.; Jawaid, A. M.; Chattopadhyay, S.; Gulec, A.; Shamirian, A.; Zuo, X.; Klie, R. F.; Schaller, R. D.; Snee, P. T. Charge Carriers Modulate the Bonding of Semiconductor Nanoparticle Dopants As Revealed by Time-Resolved X-ray Spectroscopy. *ACS Nano* **2017**, *11*, 10070–10076.

(27) Hassan, A.; Zhang, X.; Liu, C.; Snee, P. T. Electronic Structure and Dynamics of Copper-Doped Indium Phosphide Nanocrystals Studied with Time-Resolved X-ray Absorption and Large-Scale DFT Calculations. *The Journal of Physical Chemistry C* **2018**, *122*, 11145–11151.

(28) Mahl, J.; Neppl, S.; Roth, F.; Borgwardt, M.; Saladrigas, C.; Toulson, B.; Cooper, J.; Rahman, T.; Bluhm, H.; Guo, J.; Yang, W.; Huse, N.; Eberhardt, W.; Gessner, O. Decomposing electronic and lattice contributions in optical pump – X-ray probe transient inner-shell absorption spectroscopy of CuO. *Faraday Discussions* **2019**, *216*, 414–433.

(29) Harvey, S.; Houck, D.; Kirschner, M.; Flanders, N.; Brumberg, A.; Leonard, A.; Watkins, N.; Chen, L.; Dichtel, W.; Zhang, X.; Korgel, B.; Wasielewski, M.; Schaller, R. Transient Lattice Response upon Photoexcitation in CuInSe2 Nanocrystals with Organic or Inorganic Surface Passivation. *ACS Nano* **2020**, *14*, 13548–13556.

(30) Wu, Z.; Benfatto, M.; Natoli, C. R. Electronic structure and final-state effects in Nd2CuO4, La2CuO4, and Ca2CuO3 compounds by multichannel multiple-scattering theory at the copper K edge. *Physical Review B* **1996**, *54*, 13409–13412.

(31) Croft, M.; Sills, D.; Greenblatt, M.; Lee, C.; Cheong, S.-W.; Ramanujachary, K. V.; Tran, D. Systematic Mn d-configuration change in the La1–xCaxMnO3 system: A Mn K-edge XAS study. *Physical Review B* **1997**, *55*, 8726–8732.

(32) Kosugi, N.; Kondoh, H.; Tajima, H.; Kuroda, H. Cu K-edge XANES of (La1-xSrx)2CuO4, YBa2Cu3Oy and related Cu oxides. valence, structure and final-state effects on 1s-4pπ and 1s-4pσ absorption. *Chemical Physics* **1989**, *135*, 149–160.

(33) Rossi, T.; Penfold, T. J.; Rittmann-Frank, M. H.; Reinhard, M.; Rittmann, J.; Borca, C. N.; Grolimund, D.; Milne, C. J.; Chergui, M. Characterizing the Structure and Defect Concentration of ZnO Nanoparticles in a Colloidal Solution. *The Journal of Physical Chemistry C* **2014**, *118*, 19422–19430.

(34) Chiou, J. W.; Jan, J. C.; Tsai, H. M.; Bao, C. W.; Pong, W. F.; Tsai, M.-H.; Hong, I.-H.; Klauser, R.; Lee, J. F.; Wu, J. J.; Liu, S. C. Electronic structure of ZnO nanorods studied by angle-dependent x-ray absorption spectroscopy and scanning photoelectron microscopy. *Applied Physics Letters* **2004**, *84*, 3462–3464.

(35) Han, S.-W.; Yoo, H.-J.; An, S. J.; Yoo, J.; Yi, G.-C. Orientation-dependent x-ray absorption fine structure of ZnO nanorods. *Applied Physics Letters* **2005**, *86*, 021917.

(36) Zhukov, V. P.; Echenique, P. M.; Chulkov, E. V. Two types of excited electron dynamics in zinc oxide. *Physical Review B* **2010**, *82*, 094302–094308.

(37) Anspoks, A.; Kalinko, A.; Kalendarev, R.; Kuzmin, A. Local structure relaxation in nanocrystalline Ni1–xO thin films. *Thin Solid Films* **2014**, *553*, 58–62.

(38) Jonane, I.; Anspoks, A.; Aquilanti, G.; Kuzmin, A. High-temperature X-ray absorption spectroscopy study of thermochromic copper molybdate. *Acta Materialia* **2019**, *179*, 26–35.

(39) Henke, B.; Gullikson, E.; Davis, J. X-Ray Interactions: Photoabsorption, Scattering, Transmission, and Reflection at E = 50-30,000 eV, Z = 1-92. *Atomic Data and Nuclear Data Tables* **1993**, *54*, 181–342.

(40) Sezen, H.; Shang, H.; Bebensee, F.; Yang, C.; Buchholz, M.; Nefedov, A.; Heissler, S.; Carbogno, C.; Scheffler, M.; Rinke, P.; Wöll, C. Evidence for photogenerated intermediate hole polarons in ZnO. *Nature Communications* **2015**, *6*, 6901.

(41) Janotti, A.; Van de Walle, C. G. Oxygen vacancies in ZnO. *Applied Physics Letters* **2005**, *87*, 122102.

(42) Chen, H. M.; Chen, C. K.; Lin, C. C.; Liu, R.-S.; Yang, H.; Chang, W.-S.; Chen, K.-H.; Chan, T.-S.; Lee, J.-F.; Tsai, D. P. Multi-bandgap-sensitized ZnO nanorod photoelectrode arrays for water splitting: An X-ray absorption spectroscopy approach for the electronic evolution under solar illumination. *The Journal of Physical Chemistry C* **2011**, *115*, 21971–21980.

(43) Chen, H. M.; Chen, C. K.; Chen, C.-J.; Cheng, L.-C.; Wu, P. C.; Cheng, B. H.; Ho, Y. Z.; Tseng, M. L.; Hsu, Y.-Y.; Chan, T.-S.; Lee, J.-F.; Liu, R.-S.; Tsai, D. P. Plasmon Inducing Effects for Enhanced Photoelectrochemical Water Splitting: X-ray Absorption Approach to Electronic Structures. *ACS Nano* **2012**, *6*, 7362–7372.

(44) Chen, H. M.; Chen, C. K.; Tseng, M. L.; Wu, P. C.; Chang, C. M.; Cheng, L.-C.; Huang, H. W.; Chan, T. S.; Huang, D.-W.; Liu, R.-S. Plasmonic ZnO/Ag embedded structures as collecting layers for photogenerating electrons in solar hydrogen generation photoelectrodes. *Small* **2013**, *9*, 2926–2936.

(45) Lu, Y.; Wang, Y.; Chang, H.; Huang, Y.; Chen, J.; Chen, C.; Lin, Y.; Lin, Y.; Pong, W.; Ohigashi, T. Effect of Fe2O3 coating on ZnO nanowires in photoelectrochemical water splitting: A synchrotron x-ray spectroscopic and spectromicroscopic investigation. *Solar Energy Materials and Solar Cells* **2020**, *209*, 110469.

(46) Måtensson, N.; Nilsson, A. On the origin of core-level binding energy shifts. *Journal of Electron Spectroscopy and Related Phenomena* **1995**, *75*, 209–223.

(47) Šipr, O.; Šimůnek, A.; Bocharov, S.; Kirchner, T.; Dräger, G. Geometric and electronic structure effects in polarized V K-edge absorption near-edge structure spectra of V2O5. *Physical Review B* **1999**, *60*, 14115.

(48) Juhin, A.; de Groot, F.; Vankó, G.; Calandra, M.; Brouder, C. Angular dependence of core hole screening in LiCoO2: A DFT+U calculation of the oxygen and cobalt K-edge x-ray absorption spectra. *Physical Review B* **2010**, *81*, 115115.

(49) de Groot, F.; Vankó, G.; Glatzel, P. The 1s x-ray absorption pre-edge structures in transition metal oxides. *Journal of Physics: Condensed Matter* **2009**, *21*, 104207.

(50) Oshikiri, M.; Imanaka, Y.; Aryasetiawan, F.; Kido, G. Comparison of the electron effective mass of the n-type ZnO in the wurtzite structure measured by cyclotron resonance and calculated from first principle theory. *Physica B: Condensed Matter* **2001**, *298*, 472–476.

(51) Shi, S.; Xu, S. Determination of effective mass of heavy hole from phonon-assisted excitonic luminescence spectra in ZnO. *Journal of Applied Physics* **2011**, *109*, 053510.

(52) Zeller, R. Calculated core hole effects on the K X-ray spectra of BCC transition metals. *Zeitschrift für Physik B Condensed Matter* **1988**, *72*, 79–85.

(53) Bunău, O.; Joly, Y. Self-consistent aspects of x-ray absorption calculations. *Journal of Physics: Condensed Matter* **2009**, *21*, 345501.

(54) Jollet, F.; Noguera, C. Core Hole Effect on the XAS Si K Edge Shape in α-Quartz. *physica status solidi (b)* **1993**, *179*, 473–488.

(55) Gougoussis, C.; Calandra, M.; Seitsonen, A. P.; Mauri, F. First-principles calculations of x-ray absorption in a scheme based on ultrasoft pseudopotentials: From α-quartz to high-Tc compounds. *Physical Review B* **2009**, *80*, 33–38.

(56) Gulans, A.; Kontur, S.; Meisenbichler, C.; Nabok, D.; Pavone, P.; Rigamonti, S.; Sagmeister, S.; Werner, U.; Draxl, C. Exciting: a full-potential all-electron package implementing density-functional theory and many-body perturbation theory. *Journal of Physics: Condensed Matter* **2014**, *26*, 363202.

(57) Gilmore, K.; Vinson, J.; Shirley, E. L.; Prendergast, D.; Pemmaraju, C. D.; Kas, J. J.; Vila, F. D.; Rehr, J. J. Efficient implementation of core-excitation Bethe–Salpeter equation calculations. *Computer Physics Communications* **2015**, *197*, 109–117.

(58) Rehr, J. Excited state electronic structure and the theory of x-ray spectra. *Journal of Physics: Condensed Matter* **2003**, *15*, S647.

(59) Vinson, J.; Rehr, J.; Kas, J.; Shirley, E. Bethe-Salpeter equation calculations of core excitation spectra. *Physical Review B* **2011**, *83*, 115106.

(60) Özgür, Ü.; Alivov, Y. I.; Liu, C.; Teke, A.; Reshchikov, M. A.; Doğan, S.; Avrutin, V.; Cho, S.-J.; Morkoç, H. A comprehensive review of ZnO materials and devices. *Journal of Applied Physics* **2005**, *98*, 041301.

(61) Klingshirn, C.; Hauschild, R.; Fallert, J.; Kalt, H. Room-temperature stimulated emission of ZnO: Alternatives to excitonic lasing. *Physical Review B* **2007**, *75*, 115203.

(62) Hillyard, P. W.; Kuchibhatla, S. V. N. T.; Glover, T. E.; Hertlein, M. P.; Huse, N.; Nachimuthu, P.; Saraf, L. V.; Thevuthasan, S.; Gaffney, K. J. Atomic resolution mapping of the excited-state electronic structure of Cu2O with time-resolved x-ray absorption spectroscopy. *Physical Review B* **2009**, *80*, 125210–125215.

(63) Neppl, S.; Mahl, J.; Tremsin, A. S.; Rude, B.; Qiao, R.; Yang, W.; Guo, J.; Gessner, O. Towards efficient time-resolved X-ray absorption studies of electron dynamics at photocatalytic interfaces. *Faraday Discussions* **2016**, *194*, 659–682.

(64) Vura-Weis, J.; Jiang, C.-M.; Liu, C.; Gao, H.; Lucas, J. M.; de Groot, F. M. F.; Yang, P.; Alivisatos, A. P.; Leone, S. R. Femtosecond M2,3-Edge Spectroscopy of Transition-Metal Oxides: Photoinduced Oxidation State Change in α-Fe2O3. *The Journal of Physical Chemistry Letters* **2013**, *4*, 3667–3671.

(65) Lin, M.-F.; Verkamp, M. A.; Leveillee, J.; Ryland, E. S.; Benke, K.; Zhang, K.; Weninger, C.; Shen, X.; Li, R.; Fritz, D.; Bergmann, U.; Wang, X.; Schleife, A.; Vura-Weis, J. Carrier-Specific Femtosecond XUV Transient Absorption of PbI2 Reveals Ultrafast Nonradiative Recombination. *The Journal of Physical Chemistry C* **2017**, *121*, 27886–27893.

(66) Cushing, S. K.; Lee, A.; Porter, I. J.; Carneiro, L. M.; Chang, H.-T.; Zürch, M.; Leone, S. R. Differentiating photoexcited carrier and phonon dynamics in the Δ, L, and Γ valleys of Si (100) with transient extreme ultraviolet spectroscopy. *The Journal of Physical Chemistry C* **2019**, *123*, 3343–3352.

(67) Cushing, S. K.; Porter, I. J.; de Roulet, B. R.; Lee, A.; Marsh, B. M.; Szoke, S.; Vaida, M. E.; Leone, S. R. Layer-resolved ultrafast extreme ultraviolet measurement of hole transport in a Ni-TiO2-Si photoanode. *Science Advances* **2020**, *6*, eaay6650.

(68) Long, J.; Xiong, W.; Wei, C.; Lu, C.; Wang, R.; Deng, C.; Liu, H.; Fan, X.; Jiao, B.; Gao, S.; Deng, L.

Directional Assembly of ZnO Nanowires via Three-Dimensional Laser Direct Writing. *Nano Lett* **2020**, *20*, 5159–5166.

(69) Kumar, V.; Gupta, R.; Bansal, A. Hydrothermal Growth of ZnO Nanorods for Use in Dye-Sensitized Solar Cells. *ACS Applied Nano Materials* **2021**, *4*, 6212–6222.

(70) Manzeli, S.; Ovchinnikov, D.; Pasquier, D.; Yazyev, O. V.; Kis, A. 2D transition metal dichalcogenides. *Nature Reviews Materials* **2017**, *2*, 17033–17015.

(71) Yang, R.; Li, R.; Cao, Y.; Wei, Y.; Miao, Y.; Tan, W. L.; Jiao, X.; Chen, H.; Zhang, L.; Chen, Q. Oriented quasi-2D perovskites for high performance optoelectronic devices. *Advanced Materials* **2018**, *30*, 1804771.

(72) Zhang, W.; Wang, Q.; Chen, Y.; Wang, Z.; Wee, A. T. Van der Waals stacked 2D layered materials for optoelectronics. *2D Materials* **2016**, *3*, 022001.